LA-UR- 09-02234

Approved for public release; distribution is unlimited.

Title: DAMAGE PROGNOSIS OF ADHESIVELY-BONDED JOINTS IN LAMINATED COMPOSITE STRUCTURAL COMPONENTS OF UNMANNED AERIAL VEHICLES

Author(s): Maurizio Gobbato, Univ. of California, San Diego
Joel P. Conte, Univ. of California, San Diego
John B. Kosmatka, Univ. of California, San Diego
Joseph A. Oliver, Univ. of California, San Diego
Charles R. Farrar, LANL, INST-OFF

Intended for: COMPDYN 2009
ECCOMAS Thematic Conference on
Computational Methods in Structural Dynamics and
Earthquake Engineering
Rhodes, Greece, 22–24 June 2009

Los Alamos
NATIONAL LABORATORY
EST.1943

Form 836 (7/06)

COMPDYN 2009
ECCOMAS Thematic Conference on
Computational Methods in Structural Dynamics and Earthquake Engineering
M. Papadrakakis, N.D. Lagaros, M. Fragiadakis (eds.)
Rhodes, Greece, 22–24 June 2009

DAMAGE PROGNOSIS OF ADHESIVELY-BONDED JOINTS IN LAMINATED COMPOSITE STRUCTURAL COMPONENTS OF UNMANNED AERIAL VEHICLES

Maurizio Gobbato[1], Joel P. Conte[1], John B. Kosmatka[1], Joseph A. Oliver[1], and Charles R. Farrar[2]

[1] Department of Structural Engineering
University of California, San Diego
9500 Gilman Dr., La Jolla, CA 92093-0085
mgobbato@ucsd.edu, jpconte@ucsd.edu, jkosmatka@ucsd.edu, jaoliver@ucsd.edu

[2] The Engineering Institute, MS T-001
Los Alamos National Laboratory
Los Alamos, NM 87545
farrar@lanl.gov

Keywords: Damage Prognosis, Structural Health Monitoring, Probabilistic Damage Detection, Bayesian Updating, Fatigue-Induced Damage Evolution, Cohesive Zone Model.

Abstract. *The extensive use of lightweight advanced composite materials in unmanned aerial vehicles (UAVs) drastically increases the sensitivity to both fatigue- and impact-induced damage of their critical structural components (e.g., wings and tail stabilizers) during service life. The spar-to-skin adhesive joints are considered one of the most fatigue sensitive subcomponents of a lightweight UAV composite wing with damage progressively evolving from the wing root. This paper presents a comprehensive probabilistic methodology for predicting the remaining service life of adhesively-bonded joints in laminated composite structural components of UAVs. Non-destructive evaluation techniques and Bayesian inference are used to (i) assess the current state of damage of the system and, (ii) update the probability distribution of the damage extent at various locations. A probabilistic model for future loads and a mechanics-based damage model are then used to stochastically propagate damage through the joint. Combined local (e.g., exceedance of a critical damage size) and global (e.g., flutter instability) failure criteria are finally used to compute the probability of component failure at future times. The applicability and the partial validation of the proposed methodology are then briefly discussed by analyzing the debonding propagation, along a pre-defined adhesive interface, in a simply supported laminated composite beam with solid rectangular cross section, subjected to a concentrated load applied at mid-span. A specially developed Euler-Bernoulli beam finite element with interlaminar slip along the damageable interface is used in combination with a cohesive zone model to study the fatigue-induced degradation in the adhesive material. The preliminary numerical results presented are promising for the future validation of the methodology.*

1 INTRODUCTION

Probabilistic design and risk assessment methodologies for commercial, transport, and fighter aircrafts have been under development by the research community for a considerable time [1,2,3], and, more recently, the increasing use of high-performance lightweight composite materials is rendering rigorous probabilistic approaches essential. Unmanned aerial vehicles (UAVs) are a clear example of how extensively composite materials can be used in aircraft structures, and the absence of a pilot leads to higher levels of damage tolerance in the airframe. Various damage mechanisms can initiate and invisibly propagate to catastrophic levels in the most damage-sensitive UAV primary structural components. In particular, the spar-to-skin adhesive joints are recognized as one of the most fatigue-sensitive subcomponents of a lightweight composite UAV wing with the debonding process progressively evolving from the wing-root and compromising both local component/subcomponent strength and global aeroelastic performance (Bauchau and Loewy [4], and Wang *et al.* [5]).

The probabilistic framework for remaining service life prediction presented in this paper constitutes a further development and improvement of the methodology presented by the authors in a previous technical publication [6]. According to this approach, data collected during pre- and in-flight non-destructive evaluation (NDE) inspections [7] are used to assess the current state of damage of the monitored structural component (i.e., damage location, damage mechanism, and damage size). Bayesian inference is used to update the joint probability distribution function (pdf) of the damage extent at the inspected locations. A load hazard model for future aerodynamic loads and a damage evolution model are then used to stochastically propagate the damage in time. Combined local (e.g., exceedance of a critical damage size at a damage location) and global (e.g., exceedance of the flutter boundary, or initiation of limit cycle oscillation (LCO) behavior) failure criteria, similar to those used by Lin *et al.* [8] and Styuart *et. al* [9], are finally used to compute the evolution in time of the probability of *system failure* using well-established system reliability analysis methods [10].

Due to the complexity of solving the full-system problem, this study focuses on the simplified case of a composite UAV wing with the spar-to-skin adhesive joints as the only possible damageable subcomponents. Additionally, the debonding along the joints is assumed to progressively evolve from the wing root, and to be purely fatigue-driven. The propagation of damage along the adhesive interfaces is simulated using a cohesive zone model (CZM) with cyclic degradation behavior [11], fully embedded in the finite element (FE) model of the wing. Validation and calibration of the damage model with experimental fatigue test data is in progress and preliminary numerical modeling results are presented herein.

An overview of the proposed prognosis methodology is presented in the next section, and a more exhaustive description of some of its key steps is provided in Sections 3 to 6. These key steps are: Bayesian updating of the current state of damage of the monitored component, probabilistic load hazard analysis, and probabilistic structural response and damage prognosis analyses. Finally, the FE model being developed for the CZM calibration and some preliminary results, are discussed in Section 7.

2 OVERVIEW OF PROPOSED DAMAGE PROGNOSIS METHODOLOGY

The flowchart shown in Figure 1 illustrates conceptually the process of uncertainty propagation necessary to estimate the remaining service life of a UAV structural component (e.g., the UAV wing) once a new NDE inspection outcome, at time t_p, is available. The inspection outcome is represented by the measured damage size vector, $\mathbf{A}_m^p$, at the inspected locations at time t_p. In the first step of the methodology this new information is used to compute the posterior joint pdf of the actual (true) damage size vector, $\mathbf{A}_a^p$, at time t_p, conditional on the mate-

rial ($\boldsymbol{\Theta}_{mat}$) and damage model ($\boldsymbol{\Theta}_D$) parameters, and all the NDE measurements up to time t_p, denoted by $\mathbf{a}_m^{[0,p]} = \{\mathbf{a}_m^0, \mathbf{a}_m^1, ..., \mathbf{a}_m^p\}$. For sake of simplicity, this posterior joint pdf, given in full form as $f''_{\mathbf{A}_a^p|\boldsymbol{\Theta}_{mat},\boldsymbol{\Theta}_D,\mathbf{A}_m^{[0,p]}}(\mathbf{a}_a^p|\boldsymbol{\theta}_{mat},\boldsymbol{\theta}_D,\mathbf{a}_m^{[0,p]})$, is hereafter denoted $f''_{\mathbf{A}_a^p|\boldsymbol{\Theta}_{mat},\boldsymbol{\Theta}_D}(\mathbf{a}_a^p|\boldsymbol{\theta}_{mat},\boldsymbol{\theta}_D)$, without explicitly including the dependency on $\mathbf{A}_m^{[0,p]}$. Multiple damage locations and multiple damage mechanisms, evolving simultaneously at a given location, can potentially be considered by the recursive Bayesian updating procedure used herein. Both damage locations and mechanisms are uncertain, due to the inherent imperfections of NDE techniques; however, as a simplifying assumption, they are considered deterministic in this study.

The random parameter vector $\boldsymbol{\Theta}_{mat}$ exclusively describes the uncertainty in the material properties used to model the parts of the structure which are assumed to be non-damageable, while the random vector $\boldsymbol{\Theta}_D$ quantifies the uncertainty of those parameters that control the fatigue-induced material degradation in the pre-identified damageable subcomponents. For the specific case studied herein, $\boldsymbol{\Theta}_{mat}$ defines stiffness and strength parameters of (i) the composite laminated spars, and (ii) the honeycomb-core composite panels of the wing-skin, while $\boldsymbol{\Theta}_D$ characterizes the mechanical properties of the adhesive interfaces where debonding can occur—e.g., *mode I & mode II* critical fracture energies, peak shear strength, ultimate opening or sliding displacements before fracture. Since the material properties $\boldsymbol{\Theta}_{mat}$ and the adhesive interface properties $\boldsymbol{\Theta}_D$ characterize different materials, $\boldsymbol{\Theta}_{mat}$ and $\boldsymbol{\Theta}_D$ are reasonably assumed to be statistically independent (s.i.) henceforth.

The second step of the damage prognosis methodology, probabilistic load hazard analysis, defines the joint pdf of the turbulence and maneuver intensity measures ($\mathbf{IM}_T$, $\mathbf{IM}_M$), conditional on the flight profile ($\boldsymbol{\Theta}_F$) and the assumed s.i. turbulence ($\boldsymbol{\Theta}_T$) and maneuver ($\boldsymbol{\Theta}_M$) parameters. This joint pdf is denoted by $f_{\mathbf{IM}_T,\mathbf{IM}_M|\boldsymbol{\Theta}_F}(\mathbf{im}_T,\mathbf{im}_M|\boldsymbol{\theta}_F)$, and is computed by unconditioning the conditional pdf $f_{\mathbf{IM}_T,\mathbf{IM}_M|\boldsymbol{\Theta}_T,\boldsymbol{\Theta}_M,\boldsymbol{\Theta}_F}(\mathbf{im}_T,\mathbf{im}_M|\boldsymbol{\theta}_T,\boldsymbol{\theta}_M,\boldsymbol{\theta}_F)$ with respect to (w.r.t.) the parameters $\boldsymbol{\Theta}_T$ and $\boldsymbol{\Theta}_M$ (considered s.i. of $\boldsymbol{\Theta}_F$). Within the time window (or *duty cycle*) $[t_p, t_{p+1}]$—which typically encompasses several flights—an a-priori unknown number of flight segments (n_s), each of them characterized by a unique altitude of flight ($h^{(k)}$), can occur; therefore, $\boldsymbol{\Theta}_F$ collects the flight profile parameters (e.g., altitude of flight $h^{(k)}$, velocity of the aircraft $V^{(k)}$ relative to the mean stream wind velocity, duration of k^{th} flight segment $\Delta t^{(k)}$) for each of the flight segments in $[t_p, t_{p+1}]$, as $\boldsymbol{\Theta}_F = \{\boldsymbol{\Theta}_F^{(k)}, k = 1, ..., n_s\}$. As a direct consequence, $\mathbf{IM}_T$ must be defined probabilistically for each flight segment as $\mathbf{IM}_T = \{\mathrm{IM}_T^{(1)}, ..., \mathrm{IM}_T^{(n_s)}\}$.

On the other hand, $\mathbf{IM}_M$ can provide information on the mean rate of occurrence of maneuvers, their duration, and the associated peak vertical/gravity load (g-load) on the wings—

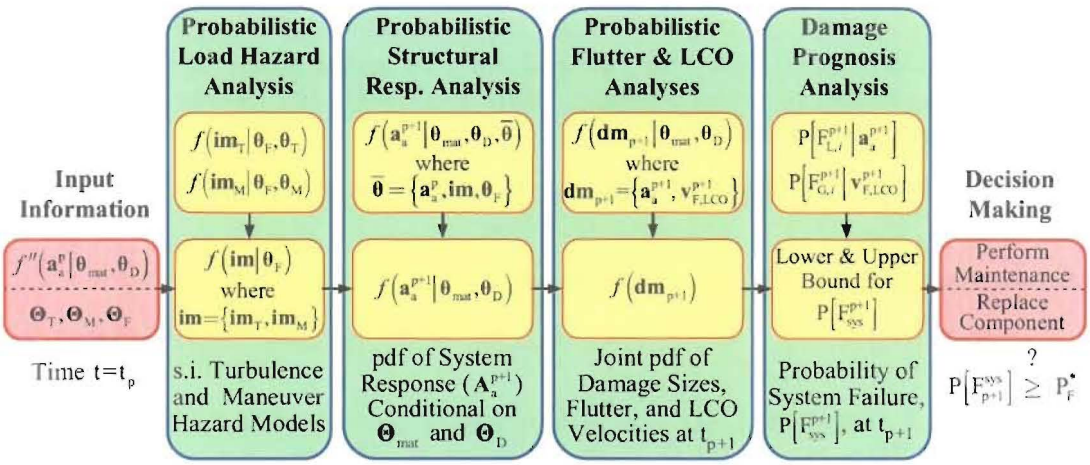

Figure 1: Overview of proposed damage prognosis methodology for remaining life prediction

as first approximation, a maneuver-induced load can in fact be thought as an increment (positive or negative) of g-load [12]. Furthermore, especially for fighter and UAV aircrafts, the occurrence of a maneuver can be reasonably considered s.i. of the atmospheric turbulence level (i.e., $\mathbf{IM}_T$ and $\mathbf{IM}_M$ are s.i.). These two intensity measures, combined together, are then used as driving sources of uncertainty for computing the aerodynamic load characteristics.

In the third step of the proposed methodology, namely probabilistic structural response analysis, the conditional pdf of the structural response of the system—in terms of the damage size vector ($\mathbf{A}_a^{p+1}$) at time t_{p+1}—is computed through extensive Monte Carlo (MC) simulations. This pdf, conditional on $\boldsymbol{\Theta}_{mat}$, $\boldsymbol{\Theta}_D$, and all the previous NDE outcomes $\mathbf{a}_m^{[0:p]}$ (not explicitly included in the notation), is denoted by $f_{\mathbf{A}_a^{p+1}|\boldsymbol{\Theta}_{mat},\boldsymbol{\Theta}_D}\left(\mathbf{a}_a^{p+1}\middle|\boldsymbol{\theta}_{mat},\boldsymbol{\theta}_D\right)$. It is worth noting that $f_{\mathbf{A}_a^{p+1}|\boldsymbol{\Theta}_{mat},\boldsymbol{\Theta}_D}\left(\mathbf{a}_a^{p+1}\middle|\boldsymbol{\theta}_{mat},\boldsymbol{\theta}_D\right)$ cannot be unconditioned with respect to $\boldsymbol{\Theta}_{mat}$ and $\boldsymbol{\Theta}_D$, at this stage of the uncertainty propagation process, since these conditioning variables are used explicitly in the next analytical step of the methodology as outlined below. The final outcome of this third step is also used as prior information for the next Bayesian updating, as the next NDE inspection outcome ($\mathbf{a}_m^{p+1}$) becomes available at time t_{p+1}.

The fourth step, namely probabilistic flutter & LCO analyses, estimates the joint pdf of the damage size vector ($\mathbf{A}_a^{p+1}$), the flutter velocity (V_F^{p+1}), and the vector of LCO velocities ($\mathbf{V}_{LCO}^{p+1}$) at time t_{p+1}—i.e., the joint pdf $f_{\mathbf{DM}_{p+1}}\left(\mathbf{dm}_{p+1}\right)=f_{\mathbf{A}_a^{p+1},V_F^{p+1},\mathbf{V}_{F,LCO}^{p+1}}\left(\mathbf{a}_a^{p+1},v_F^{p+1},\mathbf{v}_{LCO}^{p+1}\right)$ of the random vector $\mathbf{DM}_{p+1}=\left\{\mathbf{A}_a^{p+1},V_F^{p+1},\mathbf{V}_{LCO}^{p+1}\right\}=\left\{\mathbf{A}_a^{p+1},\mathbf{V}_{F,LCO}^{p+1}\right\}$. This pdf contains both local (through $\mathbf{A}_a^{p+1}$) and global (through $\mathbf{V}_{F,LCO}^{p+1}$) damage-related information and can be derived by unconditioning the conditional pdf's $f_{\mathbf{V}_{F,LCO}^{p+1}|\mathbf{A}_a^{p+1},\boldsymbol{\Theta}_{mat},\boldsymbol{\Theta}_D}\left(\mathbf{v}_{F,LCO}^{p+1}\middle|\mathbf{a}_a^{p+1},\boldsymbol{\theta}_{mat},\boldsymbol{\theta}_D\right)$ and $f_{\mathbf{A}_a^{p+1}|\boldsymbol{\Theta}_{mat},\boldsymbol{\Theta}_D}\left(\mathbf{a}_a^{p+1}\middle|\boldsymbol{\theta}_{mat},\boldsymbol{\theta}_D\right)$ w.r.t. $\boldsymbol{\Theta}_{mat}$ and $\boldsymbol{\Theta}_D$, and then using the conditional probability theorem.

Once this information is available, the probability of *system failure* at time t_{p+1}, $P\left[F_{sys}^{p+1}\right]$, can be estimated through a combination of well-established component- and system-reliability analysis methods. This task is performed in the fifth, and last, step of the framework, namely damage prognosis, through three sub-steps: (i) computation of the conditional component (or modal) failure probabilities, $P\left[F_{L,i}^{p+1}\middle|\mathbf{a}_a^{p+1}\right]$ (with $i=1,\ldots,N_L$) and $P\left[F_{G,i}^{p+1}\middle|\mathbf{v}_{F,LCO}^{p+1}\right]$ (with $i=1,\ldots,N_G$), associated with each of the N_L Local and N_G Global conditional failure modes, respectively; (ii) computation of the unconditional modal failure probabilities, $P\left[F_{L,i}^{p+1}\right]$ and $P\left[F_{G,i}^{p+1}\right]$ by unconditioning the terms $P\left[F_{L,i}^{p+1}\middle|\mathbf{a}_a^{p+1}\right]$ and $P\left[F_{G,i}^{p+1}\middle|\mathbf{v}_{F,LCO}^{p+1}\right]$ w.r.t. $\mathbf{A}_a^{p+1}$ and $\mathbf{V}_{F,LCO}^{p+1}$, respectively; and (iii) computation of lower and upper bounds for $P\left[F_{sys}^{p+1}\right]$ by abstracting the UAV wing as a series system (i.e., a system that fails if any of its "reliability" components fails). These concepts, outlined above, are described in detail in Section 6.

Using the assumptions stated, and the notation $dP[X]=P[x<X\le x+dx]=f_X(x)dx$, $dP[X,Y]=P[x<X\le x+dx\cap y<Y\le y+dy]=f_{XY}(x,y)\,dx\,dy$, and $dP[X|z]=dP[X|Z=z]=P[x<X\le x+dx|Z=z]=f_{X|Z}(x|z)\,dx$, the probability of *system failure* at time t_{p+1} can be conceptually obtained by taking advantage of the total probability theorem (TPT) multiple times in a nested fashion, as

$$P\left[F_{sys}^{p+1}\right]=\int_{\mathbf{DM}_{p+1}}P\left[F_{sys}^{p+1}\middle|\mathbf{DM}_{p+1}\right]dP\left[\mathbf{DM}_{p+1}\right]=\int_{\mathbf{A}_a^{p+1}}\int_{\mathbf{V}_{F,LCO}^{p+1}}P\left[F_{sys}^{p+1}\middle|\mathbf{A}_a^{p+1},\mathbf{V}_{F,LCO}^{p+1}\right]dP\left[\mathbf{A}_a^{p+1},\mathbf{V}_{F,LCO}^{p+1}\right],\quad(1)$$

where the term $dP\left[\mathbf{A}_a^{p+1},\mathbf{V}_{F,LCO}^{p+1}\right]$ can be expressed as

$$dP\left[\mathbf{A}_a^{p+1},\mathbf{V}_{F,LCO}^{p+1}\right]=\int_{\boldsymbol{\Theta}_{mat}}\int_{\boldsymbol{\Theta}_D}dP\left[\mathbf{V}_{F,LCO}^{p+1}\middle|\mathbf{A}_a^{p+1},\boldsymbol{\Theta}_{mat},\boldsymbol{\Theta}_D\right]dP\left[\mathbf{A}_a^{p+1}\middle|\boldsymbol{\Theta}_{mat},\boldsymbol{\Theta}_D\right]dP\left[\boldsymbol{\Theta}_{mat}\right]dP\left[\boldsymbol{\Theta}_D\right],\quad(2)$$

and the quantity $dP\left[\mathbf{A}_a^{p+1}\middle|\boldsymbol{\Theta}_{mat},\boldsymbol{\Theta}_D\right]$ can be computed by unconditioning the conditional probability $dP\left[\mathbf{A}_a^{p+1}\middle|\boldsymbol{\Theta}_{mat},\boldsymbol{\Theta}_D,\mathbf{A}_a^p,\mathbf{IM},\boldsymbol{\Theta}_F\right]$ with respect to $\mathbf{A}_a^p$, $\mathbf{IM}$, $\boldsymbol{\Theta}_F$, and accounting for the fact that $\mathbf{A}_a^p$ is s.i. of both $\mathbf{IM}$ and $\boldsymbol{\Theta}_F$, as

$$dP\left[\mathbf{A}_a^{p+1}\middle|\boldsymbol{\Theta}_{mat},\boldsymbol{\Theta}_D\right]=\int_{\mathbf{A}_a^p}\int_{\mathbf{IM}}\int_{\boldsymbol{\Theta}_F} dP\left[\mathbf{A}_a^{p+1}\middle|\boldsymbol{\Theta}_{mat},\boldsymbol{\Theta}_D,\mathbf{A}_a^p,\mathbf{IM},\boldsymbol{\Theta}_F\right]dP''\left[\mathbf{A}_a^p\middle|\boldsymbol{\Theta}_{mat},\boldsymbol{\Theta}_D\right]dP\left[\mathbf{IM}\middle|\boldsymbol{\Theta}_F\right]dP\left[\boldsymbol{\Theta}_F\right]. \tag{3}$$

Finally, the term $dP[\mathbf{IM}|\boldsymbol{\Theta}_F]$, which characterizes the future turbulence- and maneuver-induced loads in $[t_p, t_{p+1}]$, can be written as the product of two s.i. terms, as

$$dP\left[\mathbf{IM}\middle|\boldsymbol{\Theta}_F\right]=dP\left[\mathbf{IM}_T,\mathbf{IM}_M\middle|\boldsymbol{\Theta}_F\right]=\int_{\boldsymbol{\Theta}_T} dP\left[\mathbf{IM}_T\middle|\boldsymbol{\Theta}_T,\boldsymbol{\Theta}_F\right]dP\left[\boldsymbol{\Theta}_T\middle|\boldsymbol{\Theta}_F\right]\cdot\int_{\boldsymbol{\Theta}_M} dP\left[\mathbf{IM}_M\middle|\boldsymbol{\Theta}_M,\boldsymbol{\Theta}_F\right]dP\left[\boldsymbol{\Theta}_M\middle|\boldsymbol{\Theta}_F\right]. \tag{4}$$

3 PROBABILISTIC ASSESSMENT OF CURRENT STATE OF DAMAGE

Information on the current structural integrity of the UAV wing is assumed to be provided by continuous in-flight monitoring as well as more sophisticated and accurate (but less frequent) pre-flight inspections; both need therefore to be characterized probabilistically in order to assess their reliability and fidelity. The following three assumptions are made: (i) An NDE inspection can detect, locate, classify, and quantify (e.g., using an equivalent damage size) the extent of damage; (ii) The conditional inspection results (i.e., the measured extents of damage, $\mathbf{A}_m^p$, conditional on the actual damage sizes, $\mathbf{A}_a^p$) at the inspected locations, at time t_p, are s.i. events; (iii) The uncertainty in the measured extent of damage, for a given NDE technique, depends on both location and damage mechanism. These sources of uncertainty are accounted for by the following damage-size measurement model, used by Zhang and Mahadevan [13]:

$$A_m^{(i,j,p)}\left(A_a^{(i,j,p)}=a_a^{(i,j,p)}\right)=\alpha_{ij}+\beta_{ij}\,a_a^{(i,j,p)}+\varepsilon_{ij}\,, \tag{5}$$

where $A_a^{(i,j,p)}$ and $A_m^{(i,j,p)}$ (both considered as random variables) are respectively the actual and the measured damage sizes for damage location i, damage mechanism j, at time t_p; $a_a^{(i,j,p)}$ denotes a particular realization/value of the actual (and unknown) damage size; α_{ij} and β_{ij} are the coefficients of the (assumed) linear model accounting for systematic errors, intrinsic of the NDE technique employed; and $\varepsilon_{ij} \sim N(0,\sigma_{\varepsilon_{ij}})$ is the random measurement error assumed to be Gaussian distributed with zero-mean and standard deviation $\sigma_{\varepsilon_{ij}}$, and independent of the true damage size [13]. The quantities α_{ij}, β_{ij}, and $\sigma_{\varepsilon_{ij}}$ are unknown and have to be estimated—for the particular model shown in Equation (5)—through a linear regression analysis on a given set of known damage sizes, on which several measurements are performed in a controlled environment. The estimated linear regression coefficients and standard deviation of the random error are respectively denoted $\hat{\alpha}_{ij}$, $\hat{\beta}_{ij}$, and $\hat{\sigma}_{\varepsilon_{ij}}$. Once $\hat{\alpha}_{ij}$ and $\hat{\beta}_{ij}$ are determined, for a particular (i,j,p) combination, the estimated mean model response $\hat{\mu}_{A_m|A_a}^{(i,j,p)}$, conditional on the true damage size $a_a^{(i,j,p)}$, can then be derived from Equation (5) and expressed as

$$\hat{\mu}_{A_m|A_a}^{(i,j,p)}=\hat{\alpha}_{ij}+\hat{\beta}_{ij}\,a_a^{(i,j,p)}\,. \tag{6}$$

From Equations (5) and (6), it is then possible to compute the pdf of the measured damage size $A_m^{(i,j,p)}$, conditional on the true damage size $A_a^{(i,j,p)}$, as

$$f_{A_m|A_a}^{(i,j,p)}\left(a_m^{(i,j,p)}\middle|a_a^{(i,j,p)}\right)=\frac{1}{\sqrt{2\pi}\,\hat{\sigma}_{\varepsilon_{ij}}}e^{-\frac{1}{2}\left|\frac{a_m^{(i,j,p)}-\hat{\mu}_{A_m|A_a}^{(i,j,p)}}{\hat{\sigma}_{\varepsilon_{ij}}}\right|^2}=\varphi\left(a_m^{(i,j,p)},\hat{\mu}_{A_m|A_a}^{(i,j,p)},\hat{\sigma}_{\varepsilon_{ij}}\right), \tag{7}$$

and subsequently, from Equation (7), derive the relationship between the estimated model parameters ($\hat{\alpha}_{ij}$, $\hat{\beta}_{ij}$, $\hat{\sigma}_{\varepsilon_{ij}}$) and the Probability Of Detection (POD) curve, as

$$\mathrm{POD}(a_a^{(i,j,p)}) = P\left[A_m^{(i,j,p)} > 0 \,|\, A_a^{(i,j,p)} = a_a^{(i,j,p)}\right] = \Phi\left(\frac{\hat{\alpha}_{ij} + \hat{\beta}_{ij} a_a^{(i,j,p)}}{\hat{\sigma}_{\varepsilon_{ij}}}\right), \tag{8}$$

where $\Phi(\cdot)$ is the Standard Normal Cumulative Distribution Function (CDF). As clarified later in this section, Equation (7) is used to update the joint pdf of the damage size vector ($\mathbf{A}_a^p$) when the NDE inspection is capable of both detecting and measuring a certain flaw, while Equation (8) is employed when the NDE technique can only detect a certain flaw without quantifying its size (i.e., the NDE output is a binary state of damage). These considerations are also conceptually illustrated in Figure 2.

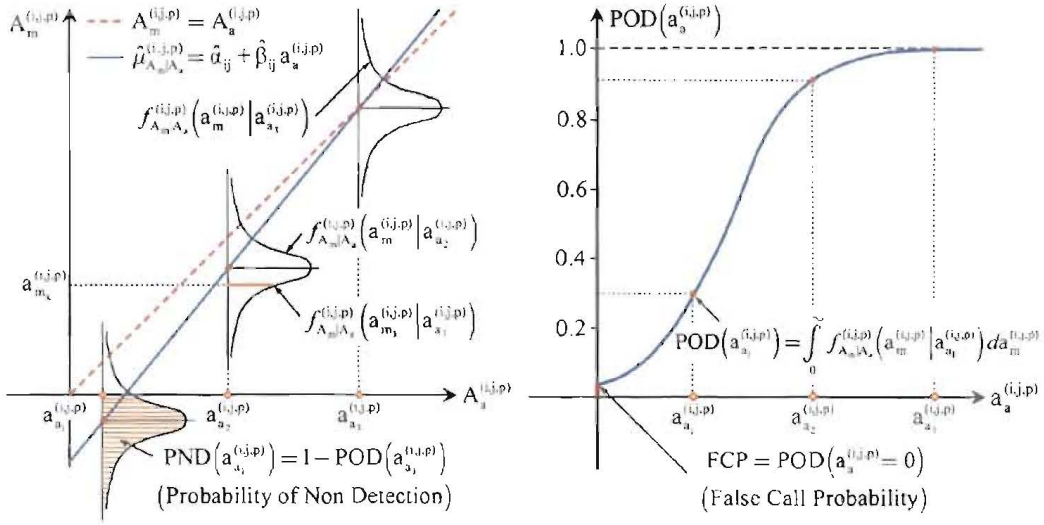

Figure 2: (a) Damage-size measurement model; (b) Example of corresponding POD curve

The Bayesian updating of the pdf of the damage size vector $\mathbf{A}_a^p$ at time t_p is based on previous work done by Zhang and Mahadevan [13], and Zheng and Ellingwood [14]. This updating process can be either performed independently for each inspected location and damage mechanism, as proposed by Lin *et al.* [8], or, more accurately and efficiently, by updating the entire prior joint pdf, $f'_{\mathbf{A}_a^p|\boldsymbol{\Theta}_{mat},\boldsymbol{\Theta}_D}(\mathbf{a}_a^p|\boldsymbol{\theta}_{mat},\boldsymbol{\theta}_D)$, obtained from the numerical simulations performed during the previous time window $[t_{p-1}, t_p]$. Using Bayes' theorem, the posterior pdf—denoted $f''_{\mathbf{A}_a^p|\boldsymbol{\Theta}_{mat},\boldsymbol{\Theta}_D}(\mathbf{a}_a^p|\boldsymbol{\theta}_{mat},\boldsymbol{\theta}_D)$—can be derived as

$$\underbrace{f_{\mathbf{A}_a^p|\boldsymbol{\Theta}_{mat},\boldsymbol{\Theta}_D,\mathbf{A}_m^{[1,p]}}\left(\mathbf{a}_a^p|\boldsymbol{\theta}_{mat},\boldsymbol{\theta}_D,\mathbf{a}_m^{[1,p]}\right)}_{f''_{\mathbf{A}_a^p|\boldsymbol{\Theta}_{mat},\boldsymbol{\Theta}_D}(\mathbf{a}_a^p|\boldsymbol{\theta}_{mat},\boldsymbol{\theta}_D)} \propto L\left(\mathbf{a}_a^p|\mathbf{a}_m^p\right) \underbrace{f_{\mathbf{A}_a^p|\boldsymbol{\Theta}_{mat},\boldsymbol{\Theta}_D,\mathbf{A}_m^{[1,p-1]}}\left(\mathbf{a}_a^p|\boldsymbol{\theta}_{mat},\boldsymbol{\theta}_D,\mathbf{a}_m^{[1,p-1]}\right)}_{f'_{\mathbf{A}_a^p|\boldsymbol{\Theta}_{mat},\boldsymbol{\Theta}_D}(\mathbf{a}_a^p|\boldsymbol{\theta}_{mat},\boldsymbol{\theta}_D)}, \tag{9}$$

and, assuming that conditional measurements outcomes—at the same (or different) damage location(s) and for the same (or different) damage mechanism(s)—are s.i. events, then Equation (9) can be rewritten as

$$f''_{\mathbf{A}_a^p|\boldsymbol{\Theta}_{mat},\boldsymbol{\Theta}_D}(\mathbf{a}_a^p|\boldsymbol{\theta}_{mat},\boldsymbol{\theta}_D) \propto \left[\prod_{i=1}^{N_L^p}\prod_{j=1}^{N_{I_i}}\prod_{k=1}^{M_n^p} L\left(a_a^{(i,j,p)}|a_{m_k}^{(i,j,p)}\right)\right] f'_{\mathbf{A}_a^p|\boldsymbol{\Theta}_{mat},\boldsymbol{\Theta}_D}(\mathbf{a}_a^p|\boldsymbol{\theta}_{mat},\boldsymbol{\theta}_D), \tag{10}$$

where, N_L^p is the number of inspected locations at time t_p (with $N_L^p \le N_L$, and N_L representing the total number of inspected locations up to time t_p), N_{T_i} is the number of detectable damage mechanisms at location i, and M_{ij}^p is the number of measurements performed at time t_p, at location i, for damage mechanism j. Furthermore, the vector $\mathbf{A}_a^p = \left\{ \mathbf{A}_a^{(i,p)},\ i=1,\ldots,N_L \right\}$ —with $\mathbf{A}_a^{(i,p)} = \left\{ A_a^{(i,j,p)},\ j=1,\ldots,N_{T_i} \right\}$—represents the collection of all the true damage sizes, while the vector $\mathbf{A}_m^p = \left\{ \mathbf{A}_m^{(i,p)},\ i=1,\ldots,N_L^p \right\}$—with $\mathbf{A}_m^{(i,p)} = \left\{ \mathbf{A}_m^{(i,j,p)},\ j=1,\ldots,N_{T_i} \right\}$ and $\mathbf{A}_m^{(i,j,p)} = \left\{ A_{m_k}^{(i,j,p)},\ k=1,\ldots,M_{ij}^p \right\}$—collects the NDE measurements at time t_p. Finally, $L\left(a_a^{(i,j,p)} \middle| a_{m_k}^{(i,j,p)}\right)$ represents the likelihood function of $a_a^{(i,j,p)}$ once the k^{th} measurement $a_{m_k}^{(i,j,p)}$ becomes available. It should be noted that: (i) the equality $L\left(\mathbf{a}_a^p \middle| a_{m_k}^{(i,j,p)}\right) = L\left(a_a^{(i,j,p)} \middle| a_{m_k}^{(i,j,p)}\right)$ is a direct consequence of the model used in Equation (5), and (ii) the mathematical form of the likelihood function depends on the measurement outcome, as

$$L\left(a_a^{(i,j,p)} \middle| a_{m_k}^{(i,j,p)}\right) = \begin{cases} \varphi\left(a_{m_k}^{(i,j,p)}, \hat{\mu}_{A_m|A_a}^{(i,j,p)}, \hat{\sigma}_{\varepsilon_{ij}}\right) & \text{if } a_{m_k}^{(i,j,p)} > 0 \\ 1 - \mathrm{POD}\left(a_a^{(i,j,p)}\right) = \mathrm{PND}\left(a_a^{(i,j,p)}\right) & \text{if } a_{m_k}^{(i,j,p)} = 0 \end{cases}, \tag{11}$$

where the mathematical condition $a_{m_k}^{(i,j,p)} = 0$ (for the k^{th} measurement) is equivalent to the event "*damage not detected*" for a given (i,j,p) combination. It must also be mentioned that: (i) the initial (i.e., before the first inspection) damage-size pdf model for $f'_{A_a^0}\left(\mathbf{a}_a^0\right)$ and its distribution parameters are chosen on the basis of engineering judgment, as pointed out also by Lin *et al.* [8], and (ii) the components of the random vector $\mathbf{A}_a^0$, at time t_0, can be reasonably considered statistically uncorrelated to each other, and s.i. of $\mathbf{\Theta}_{mat}$ and $\mathbf{\Theta}_D$. Both Lognormal and Exponential pdf models are possible and reasonable choices for $f'_{A_a^0}\left(\mathbf{a}_a^0\right)$.

3.1 Application example of proposed recursive Bayesian updating scheme

A simple application example of the proposed recursive Bayesian updating scheme, for the particular case of only two damage locations with the same damage mechanism evolving in time, is now presented. The actual damage sizes, at the two locations, are respectively denoted $A_a^{(1)}$ and $A_a^{(2)}$, and are assumed to be distributed according to a joint Lognormal pdf whose distribution parameters (i.e., mean μ, standard deviation σ, and correlation coefficient ρ) are reported in the first line of Table 1. This distribution is defined over the unbounded domain, $[0,+\infty)\times[0,+\infty)$; thus, in order to numerically apply Equation (10), $A_a^{(1)}$ and $A_a^{(2)}$ were defined over the bounded domain $[0,100]\times[0,100]\,\mathrm{mm}^2$, with the assumption that the probability content of the Lognormal pdf can be considered negligible outside of these limits. The error in the computed mean and covariance matrix of the truncated Lognormal pdf, introduced by this approximation, can be inferred from Table 1; the larger relative error is associated with the computed standard deviations of $A_a^{(1)}$ and $A_a^{(2)}$ (i.e., $\sigma_{A_a^{(1)}}$ and $\sigma_{A_a^{(2)}}$), and is of the order of 2%.

Two different damage scenarios were then considered: one with $A_a^{(1)} = A_a^{(2)} = 0.5\,\mathrm{mm}$, and a second one where the true damage sizes were set as $A_a^{(1)} = 2.5\,\mathrm{mm}$ and $A_a^{(2)} = 2.0\,\mathrm{mm}$. For each case, two series of twenty measurements (herein collected in the vectors $\mathbf{A}_m^{(1)}$, $\mathbf{A}_m^{(2)}$) were simulated, at both locations, using the model shown in Equation (6) and the parameters $\hat{\alpha}_{ij} = -1.8\,\mathrm{mm}$, $\hat{\beta}_{ij} = 1.2\,\mathrm{mm}$, and $\hat{\sigma}_{\varepsilon_{ij}} = 1.5\,\mathrm{mm}$ (with i=1, 2, and j known a priori). The measurements $\mathbf{A}_m^{(1)}$ and $\mathbf{A}_m^{(2)}$ are assumed to be taken at time t_p (the ideal case), or, more realistically, during a time window much shorter than the characteristic time scale of the damage evolution process. This assumption allows the influence of $\mathbf{\Theta}_{mat}$ and $\mathbf{\Theta}_D$ on $A_a^{(1)}$ and $A_a^{(2)}$ to be neglected. The posterior pdf's, computed from Equation (10) by either using only the measurement data $\mathbf{A}_m^{(1)}$ or both $\mathbf{A}_m^{(1)}$ and $\mathbf{A}_m^{(2)}$, are shown in Figure 3 and Figure 4, for the two damage scenarios considered. It can be noticed, especially for the first damage case

($A_a^{(1)} = A_a^{(2)} = 0.5\,\text{mm}$), how the statistical correlation in the initial prior pdf allows the uncertainty associated with $A_a^{(2)}$ to be narrowed down, even when only the measured data $\mathbf{A}_m^{(1)}$ are used in the updating process. The initial standard deviation of 2.93 mm is in fact reduced to 0.36 mm in the first damage case, and to 1.35 mm in the second one. Additionally, the statistical correlation in the posterior pdf depends on the offset of the true damage w.r.t. the region where the initial prior pdf has its highest probability content. The larger the offset, the more predominant the influence of the likelihood function over the prior knowledge. For this reason, in the second damage scenario the posterior pdf is characterized by a negligible correlation coefficient, and can be approximated by a bivariate Gaussian distribution.

Prior pdf	$\mu_{A_a^{(1)}}$ [mm]	$\mu_{A_a^{(2)}}$ [mm]	$\sigma_{A_a^{(1)}}$ [mm]	$\sigma_{A_a^{(2)}}$ [mm]	$\rho_{A_a^{(1)},A_a^{(2)}}$
Target	3.00	2.00	4.00	3.00	0.70
Truncated	2.99	2.00	3.91	2.93	0.70

Table 1: Distribution parameters of the target and the truncated joint prior Lognormal pdf's

True Damage	Measurements	$\mu_{A_a^{(1)}}$ [mm]	$\mu_{A_a^{(2)}}$ [mm]	$\sigma_{A_a^{(1)}}$ [mm]	$\sigma_{A_a^{(2)}}$ [mm]	$\rho_{A_a^{(1)},A_a^{(2)}}$
$A_a^{(1)} = 0.5\,\text{mm}$	20 @ $A_a^{(1)}$	0.43	0.40	0.22	0.36	0.48
$A_a^{(2)} = 0.5\,\text{mm}$	20 @ $A_a^{(1)}$ & $A_a^{(2)}$	0.52	0.61	0.22	0.30	0.39
$A_a^{(1)} = 2.5\,\text{mm}$	20 @ $A_a^{(1)}$	2.53	1.84	0.14	1.35	0.07
$A_a^{(2)} = 2.0\,\text{mm}$	20 @ $A_a^{(1)}$ & $A_a^{(2)}$	2.53	1.78	0.14	0.15	0.01

Table 2: Distribution parameters of the posterior pdf's after the recursive Bayesian updating procedure

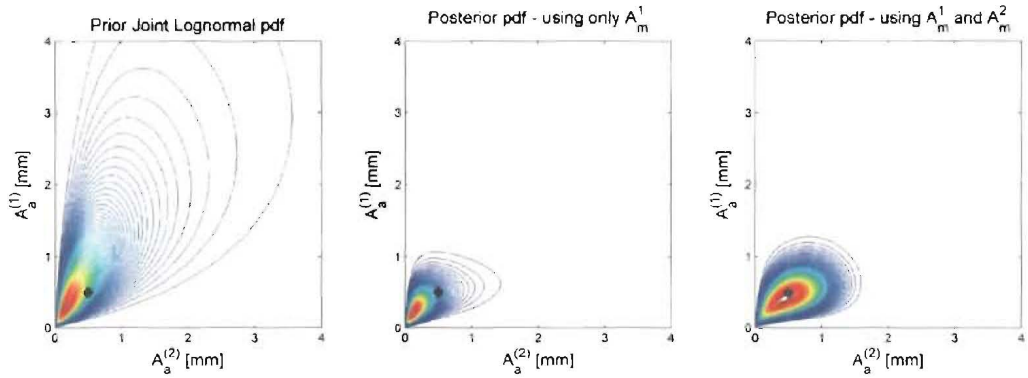

Figure 3: Prior and posterior pdf's for the damage case $A_a^{(1)} = A_a^{(2)} = 0.5\,\text{mm}$

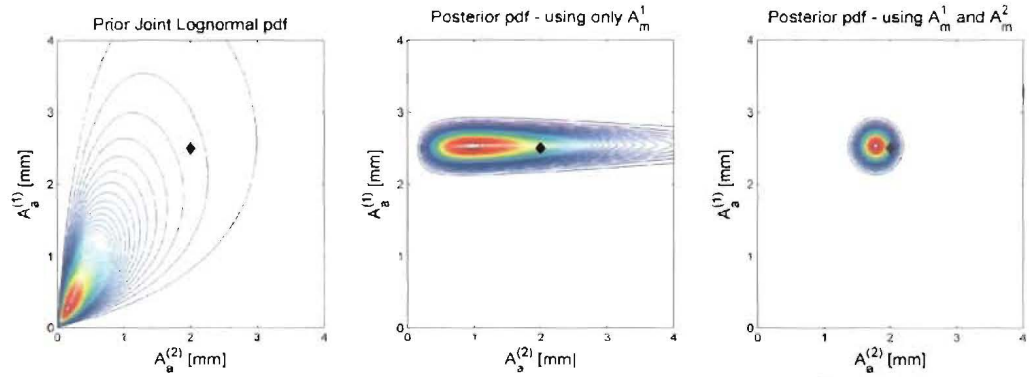

Figure 4: Prior and posterior pdf's for the damage case $A_a^{(1)} = 2.5\,\text{mm}$, $A_a^{(2)} = 2.0\,\text{mm}$

4 PROBABILISTIC LOAD HAZARD ANALYSIS

Two types of external actions are considered to primarily contribute to the damage accumulation process in the adhesive joints of a UAV wing: turbulence- and maneuver-induced loads. Turbulence is viewed as a zero-mean, isotropic, stationary (in time), and homogeneous (in space) Gaussian random velocity field, as discussed by Hoblit [15], and Van Staveren [16]. Its intensity measure ($IM_T^{(k)}$), during the k^{th} flight segment in the time window $[t_p, t_{p+1}]$, is set to be the root-mean-square (RMS) of the atmospheric turbulence velocity field ($\Sigma_T^{(k)}$). This quantity is characterized by the conditional pdf

$$f_{\Sigma_T^{(k)}|\boldsymbol{\Theta}_T,\boldsymbol{\Theta}_F^{(k)}}\left(\sigma_T^{(k)}\,|\,\boldsymbol{\theta}_T,\boldsymbol{\theta}_F^{(k)}\right)=P_0\left(h^{(k)}\right)\delta\left(\sigma_T^{(k)}\right)+\frac{P_1\left(h^{(k)}\right)}{b_1\left(h^{(k)}\right)}\sqrt{\frac{2}{\pi}}\,e^{-\frac{1}{2}\left(\frac{\sigma_T^{(k)}}{b_1\left(h^{(k)}\right)}\right)^2}+\frac{P_2\left(h^{(k)}\right)}{b_2\left(h^{(k)}\right)}\sqrt{\frac{2}{\pi}}\,e^{-\frac{1}{2}\left(\frac{\sigma_T^{(k)}}{b_2\left(h^{(k)}\right)}\right)^2}, \quad (12)$$

where $P_0\left(h^{(k)}\right)$, $P_1\left(h^{(k)}\right)$, $P_2\left(h^{(k)}\right)$, $b_1\left(h^{(k)}\right)$, and $b_2\left(h^{(k)}\right)$ are altitude-dependent distribution parameters collected in the vector $\boldsymbol{\Theta}_T$, $\delta\left(\sigma_T^{(k)}\right)$ is the Dirac delta, and the additional constraint, $P_0\left(h^{(k)}\right)=1-P_1\left(h^{(k)}\right)-P_2\left(h^{(k)}\right)$, is used to guarantee that $f_{\Sigma_T^{(k)}|\boldsymbol{\Theta}_T,\boldsymbol{\Theta}_F^{(k)}}\left(\sigma_T^{(k)}\,|\,\boldsymbol{\theta}_T,\boldsymbol{\theta}_F^{(k)}\right)$ is a proper pdf. Typical values for the turbulence distribution parameters are suggested by the Federal Aviation Regulations (FAR), and examples are shown in Figure 5. It is worth noting that $\Sigma_T^{(k)}$ is statistically dependent on $\boldsymbol{\Theta}_F^{(k)}$ exclusively through $h^{(k)}$, and, as mentioned previously, the information on $IM_T^{(k)}$ and $\boldsymbol{\Theta}_F^{(k)}$, for each flight segment, is collected in $\mathbf{IM}_T=\left\{IM_T^{(1)},\ldots,IM_T^{(n_s)}\right\}$ and $\boldsymbol{\Theta}_F=\left\{\boldsymbol{\Theta}_F^{(k)},\,k=1,\ldots,n_s\right\}$, respectively. The first contribution in the right-hand-side (RHS) of Equation (12), $P_0\left(h^{(k)}\right)\delta\left(\sigma_T^{(k)}\right)$, is normally referred to as *quiet air*, the second as *non-storm turbulence*, and the third as *storm turbulence*.

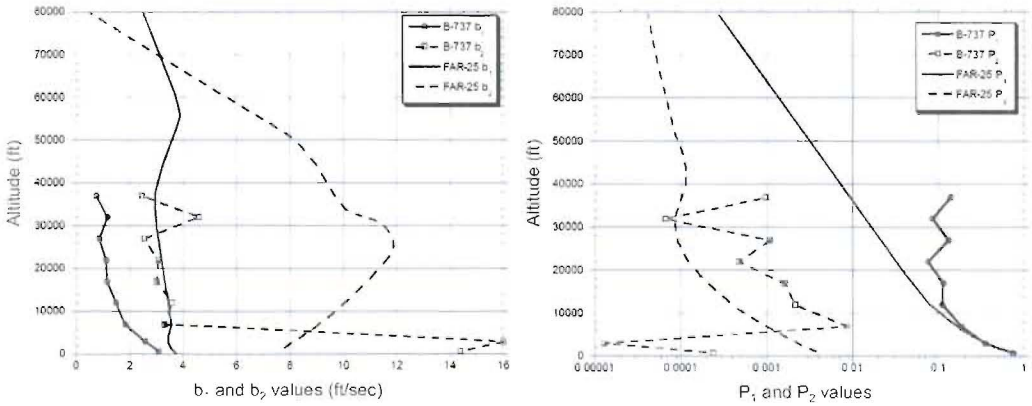

(a) (b)

Figure 5. Comparison between the turbulence distribution parameters suggested by the FAR and those experimentally derived from flight data on a Boeing 737 (B-737) aircraft: (a) b_1 and b_2; (b) P_1 and P_2.

Von Karman or Dryden turbulence velocity spectra may then be used, as detailed in reference [16], to stochastically realize 1-, 2-, or 3-D (spatially correlated) turbulence velocity fields for each flight segment. The generated turbulence paths are subsequently employed, together with the remaining flight profile information stored in $\boldsymbol{\Theta}_F$—e.g., $\left\{V^{(k)},\,k=1,\ldots,n_s\right\}$ and $\left\{\Delta t^{(k)},\,k=1,\ldots,n_s\right\}$—to generate the turbulence-induced time history loading input in $[t_p, t_{p+1}]$.

Maneuver-induced loads on a UAV wing can instead be specified, as a first approximation, by probability-of-exceedance curves of the vertical load-factor (g)—assumed to be constant during the entire time of a generic maneuver—along with the mean rate of occurrence of a maneuver per flight-hour (λ_g) and the probability distribution of maneuver-durations. All

these data are generally derived from in-flight measurements taken from similar aircrafts on similar mission profiles, and are herein collected in the random vector $\mathbf{IM}_M$. Homogeneous or non-homogeneous Poisson rectangular pulse processes [17] can be used to generate the maneuver-induced time history loading input. As stated earlier, it is assumed that the probabilistic description of a maneuver is s.i. of the level of turbulence—a reasonable assumption for UAVs which do not have an onboard pilot to react to real-time flight loads.

5 PROBABILISTIC STRUCTURAL RESPONSE ANALYSIS

Once the loading input is determined, the conditional pdf of the structural response of the system ($\mathbf{A}_a^{p+1}$) at time t_{p+1}, $f_{\mathbf{A}_a^{p+1}|\boldsymbol{\Theta}_{mat},\boldsymbol{\Theta}_D}\left(\mathbf{a}_a^{p+1}|\boldsymbol{\theta}_{mat},\boldsymbol{\theta}_D\right)$, is computed through extensive MC simulations during which the random vectors $\mathbf{A}_a^p$, $\mathbf{IM}$, and $\boldsymbol{\Theta}_F$ are simulated according to their pdf's—i.e., $f''_{\mathbf{A}_a^p|\boldsymbol{\Theta}_{mat},\boldsymbol{\Theta}_D}\left(\mathbf{a}_a^p|\boldsymbol{\theta}_{mat},\boldsymbol{\theta}_D\right)$, $f_{\mathbf{IM}|\boldsymbol{\Theta}_F}\left(\mathbf{im}|\boldsymbol{\theta}_F\right)$, and $f_{\boldsymbol{\Theta}_F}\left(\boldsymbol{\theta}_F\right)$. For this scope, a CZM for simulating the fatigue-induced damage in the adhesive joints was developed on the basis of previous work carried out by Nguyen *et al.* [11], Koutsourelakis *et al.* [18], and Tippetts and Hemez [19]. The model is characterized by (i) an envelope response, followed during monotonic loading conditions; (ii) a linear elastic unloading behavior "towards the origin", which prevents the possibility of having any residual displacement; and (iii) a progressively degrading reloading constitutive relationship, accounting for fatigue-induced damage during cycling loading, when the CZM response evolves under the envelope. The (normal and tangential) CZM traction-separation envelope curves, at a generic location/point (P) of the adhesive interface, can be expressed by the matrix Equation

$$\mathbf{T}(\mathbf{v},\lambda)=\mathbf{E}\boldsymbol{\Lambda}\mathbf{v}=\begin{bmatrix}E_n & 0\\ 0 & E_t\end{bmatrix}\begin{bmatrix}\left[1-\lambda H(v_n)\right]^{\gamma} & 0\\ 0 & (1-\lambda)^{\gamma}\end{bmatrix}\begin{Bmatrix}v_n\\ v_t\end{Bmatrix}. \tag{13}$$

In this Equation, $\mathbf{T}(\mathbf{v},\lambda)=\left\{T_n(\mathbf{v},\lambda),T_t(\mathbf{v},\lambda)\right\}^T$ is the cohesive traction vector, at point P, with its components along the normal (n) and tangential (t) directions, w.r.t. the local tangent plane of the adhesive interface at point P. The quantities $v_n=u_n/\delta_{nc}$ and $v_t=u_t/\delta_{tc}=\beta(u_t/\delta_{nc})$ are the normal and tangential relative displacements of the interface (i.e., difference between the displacements of the upper and lower adherends), normalized by their corresponding critical values δ_{nc} and δ_{tc} (i.e., the values beyond which the cohesive strength vanishes), with $\beta=\delta_{nc}/\delta_{tc}$ being the ratio between normal and tangential critical relative displacements. The two ratios $K_n^0=\left[\partial T_n/\partial u_n\right]_{u_n=0}=E_n/\delta_{nc}$ and $K_t^0=\left[\partial T_t/\partial u_t\right]_{u_t=0}=E_t/\delta_{tc}$ are the initial (normal and tangential) stiffnesses of the adhesive interface, while $\lambda=\max_{[0,t]}\sqrt[\alpha]{\left[v_nH(v_n)\right]^{\alpha}+|v_t|^{\alpha}}$ is a history-dependent damage evolution parameter, which intrinsically takes into account the instantaneous mode ratio during the whole fracture process in $[0,t]$. Finally, $H(\cdot)$ is the Heaviside function, α is a material dependent parameter ($2\le\alpha\le4$) accounting for the interaction between the three modes of fracture, and γ is a shape parameter of the CZM envelope.

It is possible to show, through some algebra (not included herein since it is beyond the scope of this article), that the proposed CZM formulation satisfies the well-established failure criterion

$$\left(\frac{G_I}{G_I^c}\right)^{\frac{\alpha}{2}}+\left(\frac{G_{II}}{G_{II}^c}\right)^{\frac{\alpha}{2}}+\left(\frac{G_{III}}{G_{III}^c}\right)^{\frac{\alpha}{2}}=1, \tag{14}$$

based on linear elastic fracture mechanics (LEFM) principles (Alfano and Crisfield, [20]). Additionally, for the particular CZM adopted, the three critical energy release rates, are related to each other as

$$G_{II}^{c}=G_{III}^{c}=\frac{G_{I}^{c}}{\beta}, \tag{15}$$

which translate into the fact that *mode II* (forward shear mode) and *mode III* (Anti plane shear mode) are indistinguishable. According again to LEFM principles, G_{I}^{c} and G_{II}^{c} must be equal to the area enclosed by the CZM envelope curves under pure *mode I* (i.e., $u_t=0$) and pure *mode II* (i.e., $u_n=0$), respectively.

The evolution of the cohesive tractions at a generic location/point (P) of the adhesive interface, during the unloading and reloading steps under the CZM envelope [11][18], is governed by the rate Equations

$$\dot{T}_i(u_i,\lambda)=\begin{cases} K_i^{u}\dot{u}_i & \text{if } \dot{u}_i<0 \\ K_i^{r}\dot{u}_i & \text{if } \dot{u}_i>0 \end{cases} \quad (i=n,t), \tag{16}$$

where the index $i=n$ refers to the normal direction (i.e., normal to the local tangent plane of the adhesive interface at P), while $i=t$ refers to the tangential direction (i.e., the projection onto the local tangent plane). The normal, and tangential, unloading (K_n^{u}, K_t^{u}), and reloading (K_n^{r}, K_t^{r}) stiffnesses in Equation (16) are assumed to evolve according to

$$K_i^{u}=T_i/u_i \tag{17}$$

$$\dot{K}_i^{r}=-\frac{1}{\delta_f}K_i^{r}\dot{u}_i \tag{18}$$

where δ_f is a characteristic opening displacement requiring experimental calibration.

Figure 6 provides a pair of simple examples to visualize the CZM envelope curves and the degrading responses under cyclic loading for the special cases of pure *mode I* and pure *mode II* fracture processes.

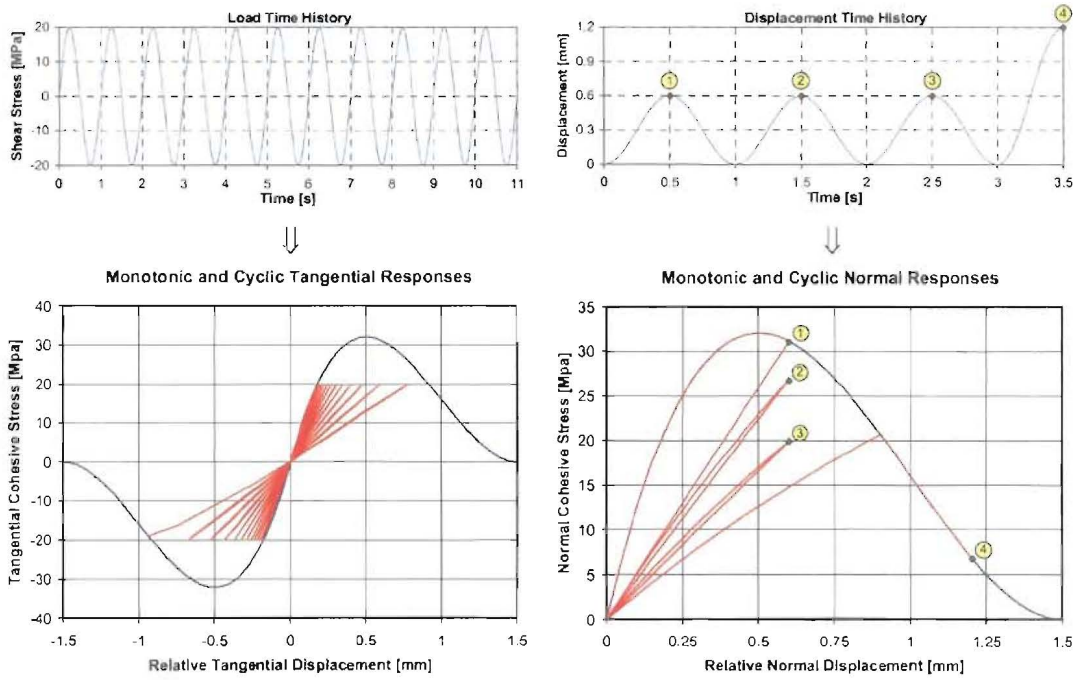

Figure 6. Degrading CZM response under cyclic loading

6 DAMAGE PROGNOSIS ANALYSIS

The last step of the proposed reliability framework—damage prognosis—can be carried out in three sub-steps by (i) using the previously computed (in the probabilistic flutter & LCO analyses step) joint pdf $f_{\mathbf{DM}_{p+1}}(\mathbf{dm}_{p+1}) = f_{\mathbf{A}_a^{p+1},\mathbf{V}_{F,LCO}^{p+1}}\left(\mathbf{a}_a^{p+1}, \mathbf{v}_{F,LCO}^{p+1}\right)$, and (ii) defining appropriate limit-states (or damage-states) capable of accounting for both local and global potential failures. The real structural system is, in this step, abstracted to a collection of reliability components linked together. Each reliability component is associated with a single limit-state (defined by a single mathematical function) and it is considered failed when the associated limit-state is reached or exceeded. This event does not necessarily reflect a physical failure.

For the simplest case in which uni-modal bounds have to be determined, the three sub-steps can be described as follows. The first step involves computing the conditional component failure probability for each (local and global) reliability component (or failure mode) considered. A local failure mode is associated with the pdf of $\mathbf{A}_a^{p+1}$ and the fidelity of the NDE technique, while a global failure mode considers the uncertainty in the random vector $\mathbf{V}_{F,LCO}^{p+1}$. As a direct consequence, the total number of local failure modes is equal to the dimension of the damage size vector $\mathbf{A}_a^{p+1}$ (denoted N_A), whereas the number of global failure modes (N_G) is equal to the size of the random vector $\mathbf{V}_{F,LCO}^{p+1}$. In general, multiple damage mechanisms can evolve simultaneously at the same location, and therefore N_A is (in general) larger than the number of inspected locations, N_L. In order to simplify the problem, however, only the failure mode (i.e., damage mechanism) with the highest failure probability is retained, at each location, in the subsequent system reliability analysis. The final number of reliability components considered is therefore equal to $N_L + N_G$, and the corresponding conditional local and global failure probabilities are denoted $P\left[F_{L,i}^{p+1} \middle| \mathbf{a}_a^{p+1}\right]$ (with $i = 1, \ldots, N_L$), and $P\left[F_{G,i}^{p+1} \middle| \mathbf{v}_{F,LCO}^{p+1}\right]$ (with $i = 1, \ldots, N_G$). In the second sub-step these conditional failure probabilities are uncontined w.r.t. $\mathbf{A}_a^{p+1}$ and $\mathbf{V}_{F,LCO}^{p+1}$, respectively, and the two outcomes are denoted $P\left[F_{L,i}^{p+1}\right]$ and $P\left[F_{G,i}^{p+1}\right]$. Finally, the third step involves the computation of lower and upper bounds for the probability of *system failure*, $P\left[F_{sys}^{p+1}\right]$, by considering the UAV wing as a series system.

The probability of failure, for a generic local failure mode (i.e., a generic detectable damage mechanism, j, evolving at a generic monitored damage location, i) at time t_{p+1}, is denoted $P\left[F_{L,ij}^{p+1}\right]$. It is evaluated according to Equation (19), and its graphical interpretation is depicted in Figure 7-a. This quantity represents the probability that the damage size, $A_a^{(i,j,p+1)}$, is greater than a pre-defined critical damage size (a_c^{ij}), and that the outcome of an NDE inspection (performed at time t_{p+1}) is less than a_c^{ij} [8]. It is worth noting that a_c^{ij} depends on both the location and the type of damage, and its magnitude is governed by residual strength and damage propagation stability considerations—generally derived from coupon test data. Strictly speaking, a_c^{ij} should be considered as well as a random variable, but, in this study, it is treated deterministically.

$$
\begin{aligned}
P\left[F_{L,ij}^{p+1}\right] &= P\left[\left(A_a^{(i,j,p+1)} \geq a_c^{ij}\right) \cap \left(A_m^{(i,j,p+1)} < a_c^{ij}\right)\right] \\
&= \int_{a_c^{ij}}^{+\infty} \left[\int_{-\infty}^{a_c^{ij}} \varphi\left(a_m^{(i,j,p+1)}, \hat{\mu}_{A_m|A_a}^{(i,j,p+1)}, \hat{\sigma}_{\varepsilon_{ij}}\right) da_m^{(i,j,p+1)} \right] f_{A_a^{(i,j,p+1)}}\left(a_a^{(i,j,p+1)}\right) da_a^{(i,j,p+1)} \\
&= \int_{a_c^{ij}}^{+\infty} \Phi\left[\frac{a_c^{ij} - \left(\hat{\alpha}_{ij} + \hat{\beta}_{ij}\, a_a^{(i,j,p)}\right)}{\hat{\sigma}_{\varepsilon_{ij}}} \right] f_{A_a^{(i,j,p+1)}}\left(a_a^{(i,j,p+1)}\right) da_a^{(i,j,p+1)} \\
&= \int_{a_c^{ij}}^{+\infty} P\left[F_{L,ij}^{p+1} \middle| a_a^{(i,j,p+1)}\right] f_{A_a^{(i,j,p+1)}}\left(a_a^{(i,j,p+1)}\right) da_a^{(i,j,p+1)}
\end{aligned}
\tag{19}
$$

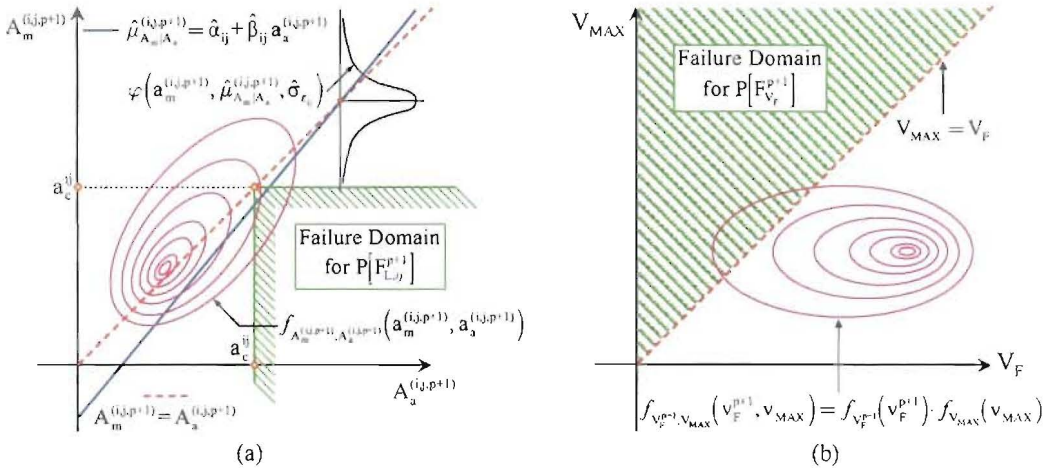

Figure 7. Failure domains according to the local and global failure criteria, respectively: (a) Exceedance of the critical damage size for a given damage location and damage mechanism; (b) Exceedance of the flutter speed, at a given future time (t_{p+1}), after damage propagation.

On the other hand the global failure criterion considers the system to be failed when the maximum operational aircraft velocity (V_{MAX}) exceeds either the reduced (due to damage) flutter (V_F^{p+1}), or any component of the LCO velocities vector ($\mathbf{V}_{LCO}^{p+1}$), at time t_{p+1}. The quantity V_{MAX} can be probabilistically described by the extreme value type I (Gumbel) distribution (Styuart *et al.*, [9]), whereas the joint pdf of V_F^{p+1} and $\mathbf{V}_{LCO}^{p+1}$, $f_{V_F^{p+1},\mathbf{V}_{LCO}^{p+1}}\left(v_F^{p+1},\mathbf{v}_{LCO}^{p+1}\right)=f_{\mathbf{V}_{F,LCO}^{p+1}}\left(\mathbf{v}_{F,LCO}^{p+1}\right)$, can be numerically computed through several flutter and LCO analyses. In this study, V_{MAX} is considered to be s.i. of both V_F^{p+1} and $\mathbf{V}_{LCO}^{p+1}$ —a reasonable assumption for UAVs because of the lack of an actual onboard pilot. Equation (20) and Figure 7-b show how this second contribution ($P\left[F_{V_F}^{p+1}\right]$), to the total probability of *system failure* ($P\left[F_{sys}^{p+1}\right]$), is computed for the particular case in which the exceedance of the flutter velocity is considered as global failure mode. Similar expressions can be used when any component of $\mathbf{V}_{LCO}^{p+1}$ is considered.

$$P\left[F_{V_F}^{p+1}\right]=P\left[V_{MAX}\geq V_F^{p+1}\right]=\int_{V_F^{p+1}}\left[1-F_{V_{MAX}}\left(v_F^{p+1}\right)\right]f_{V_F^{p+1}}\left(v_F^{p+1}\right)dv_F^{p+1} \tag{20}$$

Once all (local and global) failure modes have been analyzed, and their corresponding failure probabilities computed, it is possible to derive a lower and an upper bound for the probability of *system failure*, $P\left[F_{sys}^{p+1}\right]$, by considering the UAV wing as a series system as shown in Figure 8 below:

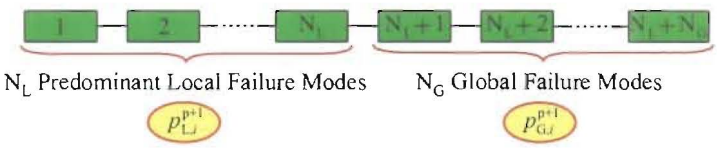

Figure 8. Conceptual representation of the UAV wing as a series system.

The key assumption in this final step, is that the evolution of multiple failure mechanisms, at the same damage location, is considered to be a fully correlated process. Therefore, only the failure mode with the highest probability of failure ($p_{L,i}^{p+1}$), herein referred to as *predominant local failure mode*, is retained in the system reliability analysis and expressed as

$$p_{L,i}^{p+1}=P\left[F_{L,i}^{p+1}\right]=\max_{j}\left(P\left[F_{L,ij}^{p+1}\right]\right)\quad i=1,\ldots,N_L\,. \tag{21}$$

Then, uni-modal Ditlevsen's bounds [10] for $P\left[F_{sys}^{p+1}\right]$, are defined as

$$\max_i\left(p_i^{p+1}\right) \le P\left[F_{sys}^{p+1}\right] \le 1-\prod_{i=1}^{N_L+N_G}\left(1-p_i^{p+1}\right), \text{ where } p_i^{p+1}=\begin{cases} p_{L,i}^{p+1} & \text{if } 1\le i\le N_L \\ p_{G,i}^{p+1} & \text{if } N_L < i \le N_L+N_G \end{cases} \quad (22)$$

where N_L represents the total number of monitored locations up to time t_p, N_G the total number of global (aeroelastic) failure modes considered, and $p_{G,i}^{p+1}$ the modal probability of failure according to the $i-N_L$ global failure mode. If a narrower confidence interval for $P\left[F_{sys}^{p+1}\right]$ is needed, then bi-modal Ditlevsen's bounds can be used. These bounds are much more difficult to compute and they are not discussed in this paper.

7 VALIDATION STRATEGY FOR THE PROPOSED FRAMEWORK

One of the key issues towards the successful application of the proposed damage prognosis methodology is represented by its validation with experimental test data on either the real structure (i.e., a UAV wing for the specific case presented herein) or a simpler, and more controllable, test structure. A crucial point in performing this task is constituted by the necessity of calibrating and validating the damage evolution model (i.e., the CZM) used in the probabilistic structural analysis step to simulate the debonding evolution along the spar-to-skin adhesive joints. The critical fracture energies (G_I^c and G_{II}^c) and the fatigue-related degradation parameter (δ_f) need therefore to be determined on the basis of experimental (static and fatigue) test data. However, the significant predominance of *mode II fracture* in the debonding evolution process along the spar-to-skin adhesive joints of a UAV wing, allows the influence of *mode I fracture* (and thus of G_I^c) to be disregarded from both the experimental and numerical modeling perspectives.

A series of end-notched flexure (ENF) static tests—conforming with ASTM standards—and three-point bending fatigue tests—aimed at estimating G_{II}^c and δ_f, respectively—were designed and are now being performed at the University of California, San Diego; the conceptual test setup for the fatigue tests is shown in Figure 9-a. It is essentially a three-point bending test on a composite laminated beam made out of two identical unidirectional carbon/epoxy adherends with the fibers aligned with the beam x-axis. The two composite laminated adherends are bonded together (after the curing process) using a common aerospace epoxy paste adhesive, Hysol® EA9394. Two initial pre-cracks are created, at the beam ends, by positioning a thin Teflon film between the adherends before bonding. Furthermore, both sinusoidal and random generated loads are considered. The specimens fabricated so far are characterized by a total span ($2L$) between 400 mm and 600 mm, a width (b) between 30 mm and 50 mm, initial pre-cracks (a) in the range of 40 mm to 80 mm (measured from the beam-end support), and identical adherends (i.e., $h_1=h_2$). The experimental fatigue test data will be used to calibrate and validate the damage model and, partially (since there is no global aeroelastic failure mode that can be considered) validate the proposed methodology. To this end, a specially de-

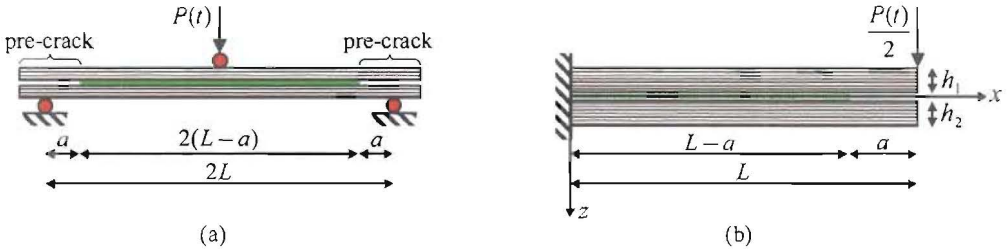

Figure 9. (a) Schematic representation of the 3-point bending fatigue test setup; (b) Beam model analyzed.

veloped Euler-Bernoulli (EB) beam finite element with interlaminar slip along a single damageable interface is used in combination with a CZM model to simulate the fatigue-induced debonding propagation observed in the experimental tests. Because of the symmetry of the test configuration, only half of the test specimen needs to be modeled (see Figure 9-b) and numerically analyzed.

7.1 Euler-Bernoulli beam element with bond slip

The formulation for two-dimensional two-layer (i.e., upper and lower adherends) composite laminated beams with nonlinear bond slip is based on previous research work [21,22] in which (i) EB beam theory (for small deformations) applies to both layers of the beam, and (ii) the deformable bonded joint is represented by an interface model (a CZM in this specific case) allowing interlayer slip and enforcing contact between the two layers of the beam (*mode I fracture* is therefore neglected by this model).

A local orthogonal reference frame $\{O; x, y, z\}$ is introduced, with the x-axis parallel to the beam axis and the vertical plane *yz* as the plane of geometrical and material symmetry of the cross section (Figure 10-a). Loads are also assumed to be symmetric w.r.t. the *yz* plane. The displacement field of a material point of the beam is given by

$$\mathbf{d}_\alpha(x,z;t)=\left[u_\alpha(x;t)+(z_\alpha-z)w'(x;t)\right]\mathbf{i}+w(x;t)\mathbf{k} \quad \text{on} \quad A_\alpha \ (\alpha=1,2), \tag{23}$$

where u_α is the axial displacement of the reference point of domain A_α, the ordinate of which is z_α ($\alpha=1$: upper adherend, $\alpha=2$: lower adherend); w is the vertical displacement of the cross section; and $\mathbf{i}$ and $\mathbf{k}$ denote the unit vectors along the x and y axes, respectively. The translational displacements (along the z-axis) and the rotations of the two layers are equal due to the enforced contact along the adhesive interface. The only nonzero strain components are the axial strain $\varepsilon_{z\alpha}$ and the bond slip s, given by

$$\varepsilon_{z\alpha}(x,z;t)=u'_\alpha(x;t)+(z_\alpha-z)w''(x;t) \quad \text{on} \quad A_\alpha \ (\alpha=1,2), \tag{24}$$

$$\mathbf{s}(x;t)=s(x;t)\mathbf{i}=\mathbf{d}_2(x,z_c;t)-\mathbf{d}_1(x,z_c;t)=\left[u_2(x;t)-u_1(x;t)+h\,w'(x;t)\right]\mathbf{i}, \tag{25}$$

where $h=z_2-z_1$ is the distance between the two reference points of each composite layer. The kinematic model presented can be used with an arbitrary thickness for each adherend; however, in order to ensure pure *mode II fracture* in the experimental tests, h_1 and h_2 must be equal [23].

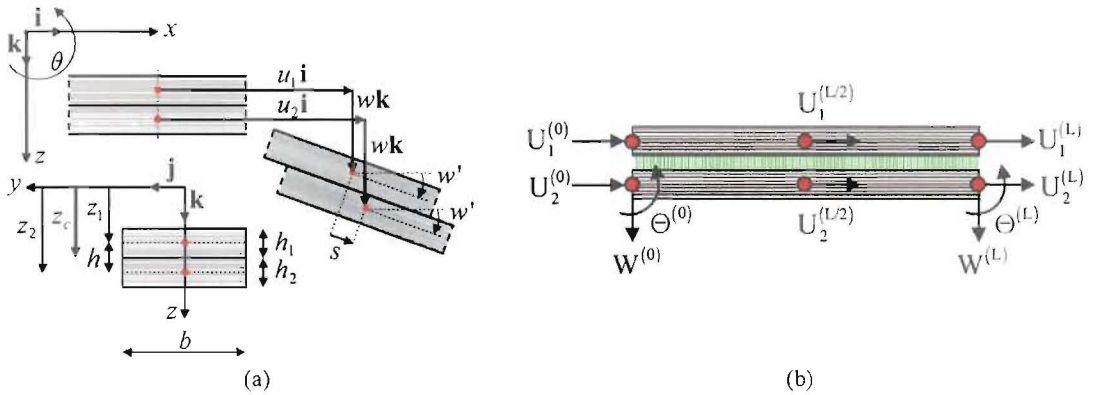

Figure 10. (a) Kinematics of the two-dimensional EB beam model with bond slip; (b) Degrees of freedom of the 10 DOF composite beam element used.

The FE formulation used in this study is a simple and effective two-dimensional ten nodal degrees-of-freedom (DOFs) displacement-based [21]. As shown in Figure 10-b, Eight DOFs are external (four for each beam end-node) and are represented by the axial displacements of upper and lower layers, the vertical displacement of the cross section and its rotation; the remaining two DOFs are internal (i.e., axial displacements of upper and lower layers). This beam element is free from shear, slip, and eccentricity locking [22]. Additionally, due to the inherent (at the section level) coupling phenomena typical of laminated composite beams and plates (e.g., bending-twisting and extension-twisting couplings), the two-dimensional beam element used is suitable to characterize the response of unidirectional and cross-ply composite laminates. This constraint has therefore to be considered together with the geometrical, material, and loading symmetry constraints mentioned earlier.

7.2 Partial verification of the proposed composite beam element

The model geometry shown in Figure 9-b and Figure 10-a, was used to performed the preliminary verification studies on the composite beam element implemented. The geometric properties were set as $L = 250\,\text{mm}$, $b = 50\,\text{mm}$, and $a = 50\,\text{mm}$. The two laminated composite adherends were assumed to be identical, with unidirectional layup and characterized by a linear elastic response ($E_{11} = 150{,}000\,\text{MPa}$ was chosen as nominal value, and is the only elastic constant needed for this particular application). The nominal mechanical properties of the CZM were assigned as $G_{ii}^{c} = 1.0\,\text{J/mm}^2$, $T_t^{max} = 50.0\,\text{MPa}$, and $\gamma = 3$. The parameter that controls the fatigue-induced degradation was instead chosen equal to $\delta_f = 0.01\,\text{mm}$ in order to have an artificially-induced faster rate of degradation (several orders of magnitude beyond the real scenario) and be thus able to reduce the computational cost of the time-history simulations during the verification process of the beam element. Additionally, various adherent thicknesses were considered during the verification phase.

Figure 11 shows the shear force profiles, along the bonded interface of the composite cantilever beam model, at three different instants of time during a dynamic time-history simulation, and for three different mesh sizes, namely 25, 50, and 100 elements. It can be easily seen

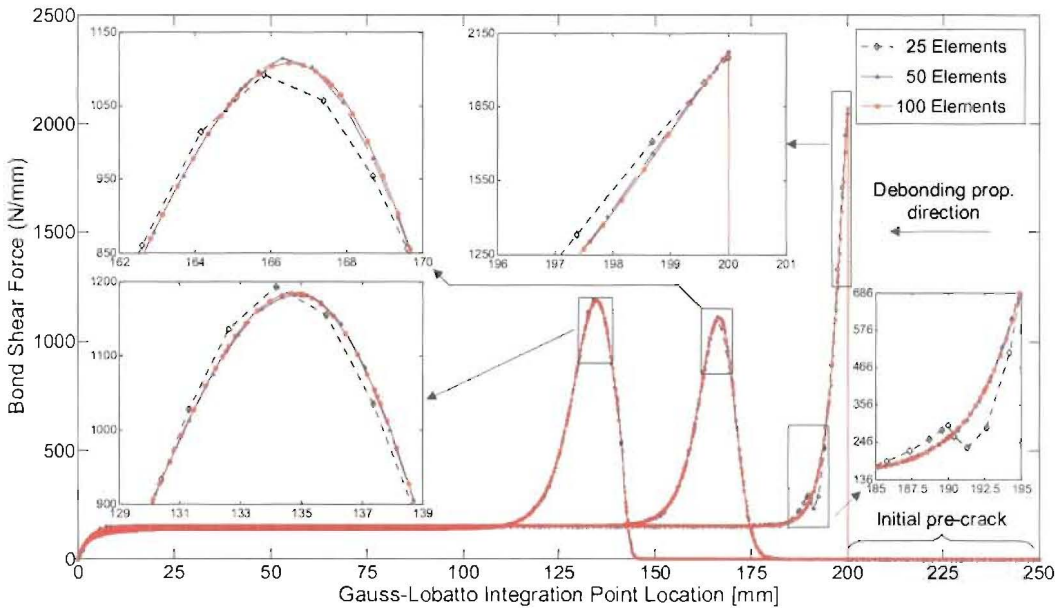

Figure 11. Shear stress profiles at three different time steps of the debonding propagation process

how the mesh refinement led to an objective (and converged) response. The stress concentration peak closer to the beam fixed-end ($x = 0\,\text{mm}$) of the cantilever beam represents the last converged time-step before the initiation of the unstable debonding propagation. In other words, also this instability (which is an actual/physical instability that can be determined analytically) is objectively captured. Similarly, Figure 12 illustrates the convergence of the CZM cyclic response at the pre-crack tip location (i.e., at 200mm from the beam fixed end). The facts discussed above are only a small part of the overall convergence and mesh objectiveness studies carried out. The influence of different combinations of (i) number of elements (i.e., different mesh sizes), (ii) number of Gauss-Lobatto integration points (within each element), (iii) integration time-step size, and (iv) load amplitude on the global (e.g., beam deflection) and local (e.g., cohesive shear force at a generic integration point) response quantities was, indeed, investigated. All the combinations analyzed led to consistent converged results.

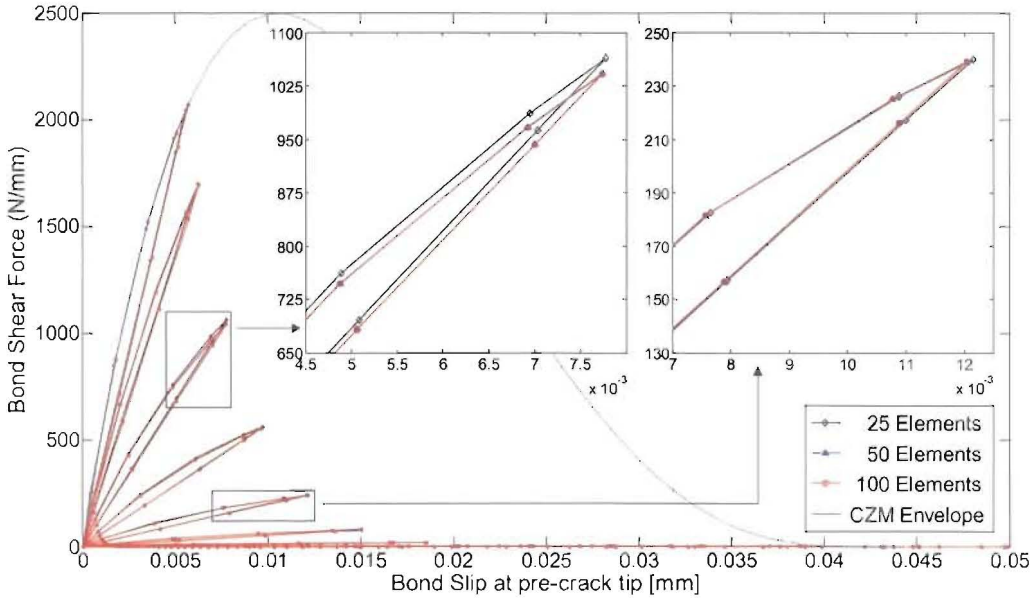

Figure 12. CZM response at the pre-crack tip (located at 200 mm from the beam fixed-end)

8 CONCLUSIONS

A reliability-based methodology for predicting the remaining useful life of a composite UAV wing has been presented. The methodology relies on continuous in-flight and periodic on-ground NDE inspections to (i) probabilistically assess and update the current state of damage of the component, and (ii) numerically propagate the probability distribution of the detected damage in time. It is assumed, based on discussions with industry UAV operators, that structural life of the wings is governed by disbonds in the spar-to-skin adhesive joints, which propagate invisibly from the wing-root. The damage process is assumed to be purely fatigue-driven, and is stochastically simulated in the methodology using a cohesive zone model (CZM), with cyclic degradation response, fully embedded in the finite element model of the wing to give estimates of the future state of damage ($\mathbf{DM}_{p+1}$) at time t_{p+1}. This information is then used, together with well-established component and system reliability methods, to compute lower and upper bounds for the probability of *system failure* accounting for both local (structural) and global (aeroelastic) failure modes. This information is used to update the maintenance plan on the basis of a predefined maximum acceptable threshold (P_F^*) for $P\left[F_{sys}^{p+1}\right]$.

Correlation and validation of the CZM model and of the overall damage prognosis methodology is in progress. Static and fatigue coupon tests on composite laminated beams are being performed in order to analyze the debonding propagation, along a pre-defined bonded joint, and to provide data for correlation. In the short term, a specially developed Euler-Bernoulli beam finite element with interlaminar slip along a single damageable interface is being used in conjunction with a CZM model to study the fatigue-induced degradation in the adhesive material and reproduce the experimental test results. Preliminary convergence and mesh-objectiveness results are presented herein, and results to date are promising. Along with finishing experimental coupon testing, a further development of the beam element, aimed at including three-dimensional and shear deformation effects, is being pursued.

9 ACKNOWLEDGMENTS

The work presented in this paper is part of an ongoing research project funded by the Educational Collaboration between Los Alamos National Laboratory and UCSD on "A Damage Prognosis System for Unmanned Aerial Vehicles". The authors wish to thank Dr. Gyuhae Park, Dr. Francois Hemez, and Mr. Trevor Tippets of the Los Alamos National Laboratory for the valuable technical discussions.

REFERENCES

[1] J.N. Yang, and W.J. Trapp, Reliability analysis of aircraft structures under random loading and periodic inspection, *AIAA Journal*, **12**(12), 1623-1630, 1974.

[2] G. Deodatis, H. Asada, and S. Ito, Reliability of aircraft structures under non-periodic inspection: a bayesian approach, *Engineering Fracture Mechanics*, **53**(5), 789-805 1996.

[3] K.Y. Lin, and A.V. Styuart, Probabilistic approach to damage tolerance design of aircraft composite structures, *Journal of Aircraft*, **44**(4), 1309-1317, 2007.

[4] O.A. Bauchau, and R.G. Loewy, *Nonlinear aeroelastic effects in damaged composite aerospace structures*, Technical Report, School of Aerospace Engineering, Georgia Institute of Technology, Atlanta, GA, 1997.

[5] K. Wang, D.J. Inman, and C.R. Farrar, Crack-induced changes in divergence and flutter of cantilevered composite panels, *Structural Health Monitoring*, **4**(4), 377-392, 2005.

[6] M. Gobbato, J.P. Conte, J.B. Kosmatka, J.A. Oliver, and C.R. Farrar, Reliability-based framework for damage prognosis of composite unmanned aerial vehicles structural components, *The Inaugural International Conference of the Engineering Mechanics Institute (EM08)*, Minneapolis, MN, USA, May 18-21, 2008.

[7] F. Lanza di Scalea, H.M. Matt, I. Bartoli, S. Coccia, G. Park, and C.R. Farrar, Health monitoring of UAV spar-to-skin joints using guided waves and macro fiber composite transducers. *Journal of Intelligent Material Systems and Structures*, **18**(4), 373-388, 2007.

[8] K.Y. Lin, J. Du, and D. Rusk, *Structural design methodology based on concepts of uncertainty*, NASA/CR-2000-209847, NASA Langley Research Center, Hampton, VA, 2000.

[9] A.V. Styuart, M. Mor, E. Livne, and K.Y. Lin., Aeroelastic failure risk assessment in damage tolerant composite airframe structures, *48th AIAA/ASME/ASCE/AHS/ASC Structures, Structural Dynamics, and Materials Conference*, Honolulu, Hi, April 23-26,2007.

[10] O. Ditlevsen and H.O. Madsen, *Structural reliability methods*, Wiley, West Sussex, England, 1996.

[11] O. Nguyen, E.A. Repetto, M. Ortiz, and R.A. Radovitzky, A cohesive model of fatigue crack growth, *International Journal of Fracture*, **110**(4), 351-369, 2001.

[12] J.W. Rustenburg, D. Skinn, and D.O. Tipps, An evaluation of methods to separate maneuver and gust load factors from measured acceleration time histories, U.S. Department of Transportation, Federal Aviation Administration, Report n. DOT/FAA/AR-99/14, 1999.

[13] R. Zhang, and S. Mahadevan, Fatigue reliability analysis using non-destructive inspection, *Journal of Structural Engineering*, **127**(8), 957-965, 2001.

[14] R. Zheng, and B.R. Ellingwood, Role of non-destructive evaluation in time-dependent reliability analysis, *Structural Safety*, **20**(4), 325-339, 1998.

[15] F.M. Hoblit, *Gust Loads on Aircraft: Concepts and Applications*, AIAA Ed. Series, Washington, D.C., 1988.

[16] W.H Van Staveren, *Analyses of aircraft responses to atmospheric turbulence*, Ph.D. Dissertation, Department of Aerospace Design, Integration & Operations, Delft University of Technology, The Netherlands, 2003.

[17] Y.-K. Wen, *Structural loading modeling and combination for performance and safety evaluation*, Elsevier, 1990.

[18] P.S. Koutsourelakis, K. Kuntiyawichai, and G.I. Schueller, Effect of Material Uncertainties on Fatigue Life Calculations of Aircraft Fuselages: a Cohesive Element Model, *Engineering Fracture Mechanics*, **73**(9), 1202-1219, 2005.

[19] T.B. Tippetts, and F.M. Hemez, Non-Linear Models of Composite Laminates, *23rd SEM International Modal Analysis Conference* (IMAC-XXIII), Orlando, FL, USA, January 31 - February 3, 2005.

[20] G. Alfano, and M.A. Crisfield, Finite element interface models for the delamination analysis of laminated composites: mechanical and computational issues, *International Journal for Numerical Methods in Engineering*, **50**(7), 1701-1736, 2001.

[21] A. Dall'Asta, and A. Zona, Nonlinear analysis of composite beams by displacement approach, *Computer & Structures*, **80**(27-30), 2217-2228, 2002.

[22] A. Dall'Asta, and A. Zona, Slip locking in finite elements for composite beams with deformable shear connection, *Finite Element in Analysis and Design*, **40**(13-14), 1907-1930, 2004.

[23] S. Hashemi, A.J. Kinloch, and J.G. Williams, The analysis of interlaminar fracture in uniaxial fibre-polymer composites, *Proceedings of the Royal Society of London, Series A, Mathematical and Physical Sciences*, **427**(1872), 173-199, 1990.